Thermal Spray 2007: Global Coating Solutions
(Ed.) B.R. Marple, M.M. Hyland, Y.-C. Lau, C.-J. Li, R.S. Lima, and G. Montavon
Published by ASM International®, Materials Park, Ohio, USA, Copyright© 2007

Sintering Kinetics of Plasma-Sprayed Zirconia TBCs

A. Cipitria, I.O. Golosnoy, T.W. Clyne
Department of Materials Science and Metallurgy, University of Cambridge, Cambridge, UK

Abstract

A model of the sintering exhibited by EB-PVD TBCs, based on the principles of free energy minimization, was recently published by Hutchinson et al [1]. In the current paper, this approach is applied to the sintering of plasma-sprayed TBCs and comparisons are made with experimental results. Predictions of through-thickness shrinkage and changing pore surface area are compared with experimental data obtained by dilatometry and BET analysis respectively. The sensitivity of the predictions to initial pore architecture and material properties are assessed. The model can be used to predict the evolution of the contact area between overlying splats. This is in turn related to the through-thickness thermal conductivity, using a previously-developed analytical model [2].

Introduction

Thermal barrier coatings (TBCs) usually comprise a metallic bond coat (e.g., MCrAlY), which protects the base metal against oxidation and corrosion and improves the adhesion of the top coat. The top coat is commonly based on zirconia stabilized by 8wt% yttria (ZrO_2-8wt%Y_2O_3) and is produced by air plasma spray (APS) or electron beam physical vapour deposition (EB-PVD). Coating thickness is usually in the range of 100-500 μm, creating a temperature drop of ~50-200ºC. TBCs are used in aero-engine and power generation gas turbine components subjected to high temperature, such as blades and nozzle guide vanes. Currently-sought increases in turbine entry temperature are dependent on improvements in the efficiency and reliability of TBCs.

APS coatings contain interlamellar pores, globular voids and intrasplat microcracks. These are partly responsible for the low thermal conductivity (k~1 W m^{-1} K^{-1}) and low global modulus (E~25 GPa) of these coatings, the latter being beneficial in reducing the stresses arising from differential thermal contraction. Under service conditions, however, TBCs are exposed to high temperatures for extended periods, leading to sintering effects. Healing of microcracks, improved intersplat bonding and grain growth can raise both the thermal conductivity and modulus, degrading both the insulation offered and the thermo-mechanical stability of the TBC. In this paper, a model is presented for the sintering of plasma-sprayed (PS) TBCs.

General Framework

The microstructure of PS TBCs is represented as cylindrical disks (splats) of radius r_{s0} and height 2 y_{s0}, with a cylindrical bridge contact of radius r_{b0} and open pore dimension 2 y_{b0} (see Fig. 1). Due to symmetry, the volume of the modeled unit cell corresponds to half-height of the splat, y_{s0}, and half-height of the pore, y_{b0}. The splats are composed of columnar grains, modelled as hexagonal prisms of side r_{g0}. A horizontal grain boundary (inter-splat contact area) is located at the mid-height of the bridge. The geometry is based on cylindrical coordinates (r^g, z^g). The through-thickness direction is along z^g, with the origin located at the interface with the substrate. The temperature distribution is taken to be isothermal at any given value of z^g, but can vary in the through-thickness direction. However, in the current work, the temperature is assumed uniform within the modelled domain. Modelled domains are assumed to tesselate in a hexagonal in-plane array and to stack on top of each other in the through-thickness direction. The space between the close-packed array of cylinders (comprising about 8% of the total volume), which is outside the modelled domain, is taken to represent porosity inaccessible to the influence of sintering phenomena. In practice, some relatively large scale, equiaxed porosity is commonly present, at approximately this level.

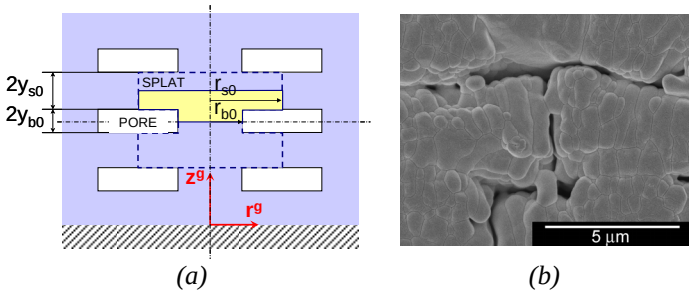

(a) *(b)*

Figure 1: Model (a) and SEM micrograph (b) of PS TBC.

As sintering proceeds (Fig. 2), surface diffusion contributes to spherodization of pores, resulting in an increase of the open pore dimension, y_b, and a decrease of the splat height, y_s. Grain boundary diffusion, on the other hand, causes the coating to shrink in the through-thickness and in-plane directions, reducing the height from the centre of the bridge to the centre of the splat, h, and the splat radius, r_s. Grain growth is not incorporated in the modelling presented here and the number of grains within each splat, N_s, is assumed to remain constant.

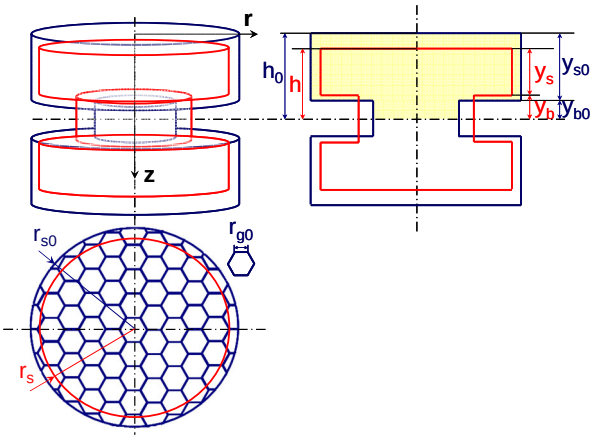

Figure 2: Perspective, plan and elevation views of the initial (blue) and later (red) dimensions of the modelled domain.

Microstructural evolution is described by the changing values of the three independent parameters: h, y_s and r_s. By mass conservation, y_b and r_b can be expressed as a function of these:

$$y_b\left(h, y_s, r_s\right) = h - y_s \tag{1}$$

$$r_b\left(h, y_s, r_s\right) = \left[\frac{r_{b0}^2 y_{b0} + r_{s0}^2 y_{s0} - r_s^2 y_s}{h - y_s}\right]^{1/2} \tag{2}$$

The volume of material corresponding to a unit cell is:

$$Vol = \pi\left(r_{s0}^2 y_{s0} + r_{b0}^2 y_{b0}\right) \tag{3}$$

The Variational Principle

The variational principle is a well established theoretical tool that has been applied to various physical problems, including diffusional void growth and crack propagation [3] [4], grain growth [5], creep deformation [4] [6], morphological evolution of electronic thin films [7] and solid-state sintering [1] [4] [8]. At a given temperature, if the atoms have enough mobility, they diffuse along free surfaces, grain boundaries and through the lattice, so as to reduce the total free energy. Energy is dissipated during mass transport, because atoms must overcome internal friction forces. A balance is established between the rates of free energy reduction and energy dissipation. A function is derived, which includes the free energy and the dissipation energy term, and the system progresses in the way to keep the function at minimum.

Formulation of the solid-state sintering problem, using the variational principle, is described elsewhere [9] [10]. The current model represents a free-standing coating, with fully interconnected porosity. Thus, there are no contributions to the free energy from either the stored elastic strain energy or the pressure acting on free surfaces. The free energy per unit volume $\overline{G}\left[\mathrm{Jm^{-3}}\right]$ is given by:

$$\begin{aligned}\overline{G}\left(h, y_S, r_S\right) &= \frac{1}{Vol}\left[\int_{A_S} \gamma_S dA_S + \int_{A_{gb}} \gamma_{gb} dA_{gb}\right] \\ &= \frac{1}{Vol}\left[\gamma_s\left(\pi\left(r_s^2 - r_b^2\right) + 2\pi r_b y_b\right) + \right. \\ &\left. + \gamma_{gb}\left(\frac{1}{2}\pi r_b^2 + \sqrt{2\sqrt{3}\pi N_s}\, r_s\left(y_s + \frac{r_b^2}{r_s^2} y_b\right)\right)\right]\end{aligned} \tag{4}$$

The factor of ½ arises because the energy of the horizontal gb, at the contact bridge, is divided between the top and bottom parts. Assumed paths of material diffusion are along gb's and free surfaces. Lattice diffusion and grain growth are not treated in the version of the model presented here. The rate of energy dissipation per unit volume $\overline{\Psi}\left[\mathrm{J\ s^{-1}\ m^{-3}}\right]$ is:

$$\begin{aligned}\overline{\Psi}\left(\dot{h}, \dot{y}_s, \dot{r}_s\right) &= \frac{1}{Vol}\left[\int_{A_s} \frac{1}{2M_s\Omega\delta_s} J_s^* J_s^* dA_s + \right. \\ &\left. + \int_{A_{gb}} \frac{1}{2M_{gb}\Omega\delta_{gb}} J_{gb}^* J_{gb}^* dA_{gb}\right]\end{aligned} \tag{5}$$

where Ω is the atomic volume; $J^*\left[\mathrm{m^3\ m^{-1}\ s^{-1}}\right]$ is the volumetric flux per unit depth, δ is the layer thickness through which diffusion takes place and $M\left[\mathrm{m^2\ J^{-1}\ s^{-1}}\right]$ is the atomic mobility. The subscripts gb and s refer to grain boundary and free surface, respectively. The atomic mobility is given by:

$$M = \frac{D_0 \exp\left(-Q/RT\right)}{k_B T} \tag{6}$$

where D_0 is the diffusivity, Q is the activation energy, k_B is the Boltzman constant, R is the gas constant and T is the absolute temperature.

Matter conservation is satisfied by relating the flux along an interface to the normal velocity of that interface:

$$\nabla \cdot \overline{J} + v_{\perp} = const \tag{7}$$

where the constant equals to zero if there are no additional sources or sinks for material from the bulk. Figure 3 depicts material fluxes along the interfaces, normal velocity of those interfaces and the existence of additional sources or sinks of material. The flux along the *z* coordinate is given by the flow of material along the vertical grain boundaries, $J^*_{gb\_V}$, with a normal velocity of the interface $\sqrt{3}\dot{r}_g = \sqrt{3}\sqrt{2\pi/3\sqrt{3}N_s}\,\dot{r}_s$ and with no source or sink of additional material. The flux along the *r* coordinate is divided into two regions: grain boundary diffusion along the horizontal grain boundary, $J^*_{gb\_H}$ (r=[0, r_b]) and surface diffusion along the pore free surface, J^*_s (r=[r_b, r_s]). The former, with a normal velocity of the interface $\dot{h}$, has a source of additional material coming from the vertical grain boundaries $\dot{h}\left(\dot{r}_s\right) = -2h\dot{r}_s/r_s$. The latter, with a normal velocity of the interface $\dot{y}_s$, has a source of additional material coming from the vertical grain boundaries $\dot{y}_s\left(\dot{r}_s\right) = -2y_s\dot{r}_s/r_s$.

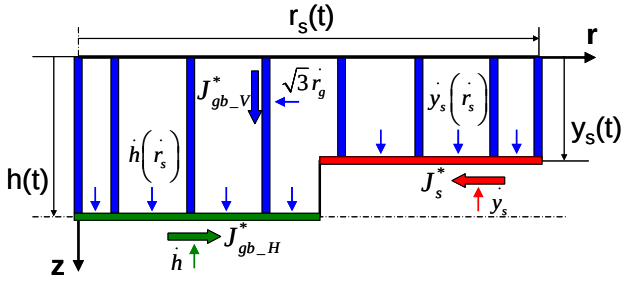

Figure 3: Schematic depiction of the diffusion paths along interfaces and the migration velocities of interfaces.

Migration velocities of the interfaces are assumed uniform along the interface. Fluxes can thus be expressed:

$$J^*_{gb\_V}(z) = -\sqrt{\frac{2\pi}{\sqrt{3}N_s}}\,\dot{r}_s\, z \tag{8}$$

$$J^*_{gb\_H}(r) = -\frac{r}{2}\left(\frac{2h}{r_s}\dot{r}_s + \dot{h}\right) \quad r = [0, r_b] \tag{9}$$

$$J^*_s(r) = \frac{1}{2}\frac{r_s^2 - r^2}{r}\left(\frac{2y_s}{r_s}\dot{r}_s + \dot{y}_s\right) \quad r = [r_b, r_s] \tag{10}$$

with the boundary conditions:

$$J^*_{gb\_V}(z=0) = 0 \quad J^*_{gb\_H}(r=0) = 0 \quad J^*_s(r=r_s) = 0 \tag{11}$$

The dissipation rate per unit volume is given by:

$$\overline{\Psi}\left(\dot{h}, \dot{y}_s, \dot{r}_s\right) = \frac{1}{Vol}\left[C_{26}\dot{h}^2 + C_{25}\dot{y}_s^2 + \right.$$
$$+\left(C_{25}\left(\frac{2y_s}{r_s}\right)^2 + C_{26}\left(\frac{2h}{r_s}\right)^2 + C_{27}\right)\dot{r}_s^2 + \tag{12}$$
$$\left. + C_{25}\frac{4y_s}{r_s}\dot{r}_s\dot{y}_s + C_{26}\frac{4h}{r_s}\dot{r}_s\dot{h}\right]$$

with

$$C_{25} = \frac{\pi}{4M_s\Omega\delta_s}\left(r_s^4 \ln\frac{r_s}{r_b} - r_s^2\left(r_s^2 - r_b^2\right) + \frac{r_s^4 - r_b^4}{4}\right)$$
$$C_{26} = \frac{\pi}{16M_{gb}\Omega\,\delta_{gb}/2}r_b^4 \tag{13}$$
$$C_{27} = \frac{\pi}{3M_{gb}\Omega\delta_{gb}}\sqrt{\frac{2\pi}{\sqrt{3}N_s}}\frac{1}{r_s}\left(r_b^2h^3 + \left(r_s^2 - r_b^2\right)y_s^3\right)$$

The variational principle [9] [10] states that, of all possible diffusive fluxes, the actual gb migration velocities and strain rates will be those minimizing the functional $\Pi = \dot{G} + \Psi$.

$$\delta\overline{\Pi} = \delta\left(\dot{\overline{G}} + \overline{\Psi}\right) = 0 \tag{14}$$

$\dot{G}$ is an explicit linear function of the rate of change of the geometrical variables and Ψ is an explicit quadratic function. Evolution of the microstructure is dictated by the rates of change of the architecture that minimize the functional:

$$\overline{\Pi}\left(\dot{h}, \dot{y}_s, \dot{r}_s\right) = \dot{\overline{G}}\left(\dot{h}, \dot{y}_s, \dot{r}_s\right) + \overline{\Psi}\left(\dot{h}, \dot{y}_s, \dot{r}_s\right) \tag{15}$$

By time integration, using the 4th order Runge-Kutta method, the time evolution of the geometrical variables is obtained.

Model Predictions

Table 1 summarizes the input data used. The parameters describing the geometry have been obtained experimentally, using mercury intrusion porosimetry and measurements on scanning electron microscope (SEM) micrographs. The surface diffusivity and activation energy are those reported for tetragonal ZrO_2-3mol%Y_2O_3 [11], while grain boundary diffusivities are for tetragonal 14CeO_2-86($Zr_{1-x}Hf_x$)O_2, with

x=0.02 and 0.10 [12]. Ω is the volume of the unit cell, calculated from lattice parameters obtained by X-ray diffraction (XRD). δ_s is taken as $\Omega^{1/3}$ and δ_{gb} as $2\Omega^{1/3}$.

Table 1: Input geometrical and material property data.

Geometry			Material properties			
		Unit			Unit	Source
r_{b0}	1.50E-06	m	D_{s0}	5.52E+05	$m^2 s^{-1}$	[11]
r_{s0}	5.00E-06	m	Q_s	5.31E+05	J mol^{-1}	[11]
y_{b0}	1.00E-07	m	D_{gb0}	4.48E+02	$m^2 s^{-1}$	[12]
y_{s0}	1.25E-06	m	Q_{gb}	5.06E+05	J mol^{-1}	[12]
r_{g0}	5.00E-07	m	γ_s	0.30	J m^{-2}	[13]
			γ_{gb}	0.15	J m^{-2}	
			Ω	3.38E-29	m^3	
			δ_s	3.23E-10	m	
			δ_{gb}	6.47E-10	m	

The model captures a number of experimentally-observed sintering trends. Sintering causes pores to spherodize, the open pore dimension y_b to increase, the contact area r_b to increase and the total pore surface area to decrease (Fig. 4).

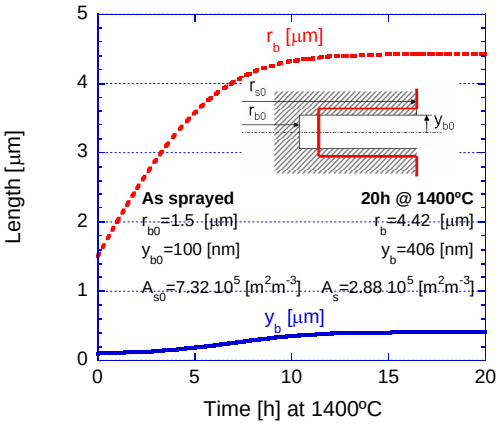

Figure 4: Predicted changes with time of r_b and y_b.

Sensitivity to Initial Pore Geometry

Figure 5 compares experimental through-thickness shrinkage data, for low impurity ZrO_2-8wt%Y_2O_3 at 1400ºC, with model predictions. The observed fall-off in shrinkage rate with increasing time is correctly predicted. The behaviour is sensitive to initial pore geometry. Predictions are shown for two pores of the same initial volume, but different pore surface area. Larger initial pore surface area leads to greater through-thickness shrinkage.

Figure 6 compares experimental surface area changes, measured using the Brunauer-Emmett-Teller (BET) adsorption isotherm [14], with predicted surface area changes, for low impurity ZrO_2-8wt%Y_2O_3 at 1400ºC. The surface area reduction is also sensitive to initial pore geometry. Predictions are given for two pores of the same initial surface area. The final surface area and the rate of surface area reduction are very sensitive to the ratio of y_b to r_b. Geometries with finer open pore dimension, y_b, spherodize faster and lead to greater pore surface area reductions.

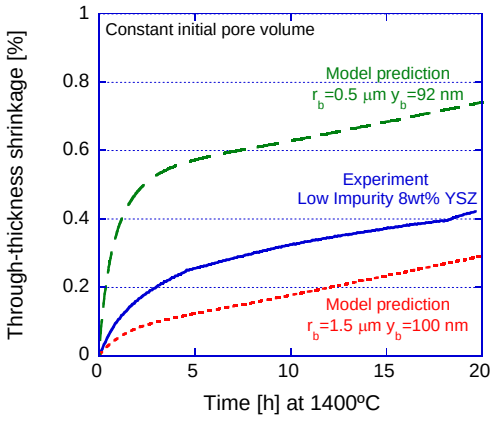

Figure 5: Comparison between predicted and observed shrinkage for low impurity ZrO_2-8wt%Y_2O_3 at 1400ºC in the through-thickness direction.

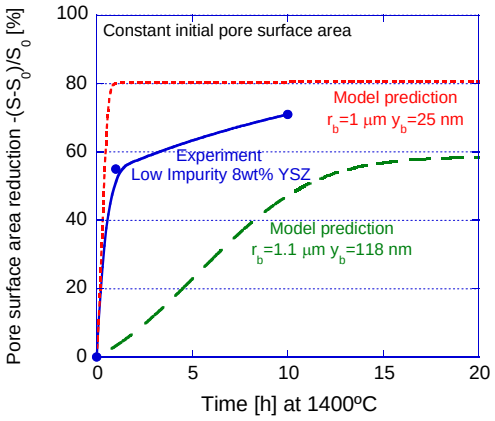

Figure 6: Comparison between predicted and observed surface area reductions at 1400ºC.

Sensitivity to Material Properties

Sintering is sensitive to surface and gb diffusivities. Surface diffusion has the effect of reducing the surface area, without causing densification. Grain-boundary diffusion reduces both pore surface area and specimen volume. Through-thickness shrinkage (Fig. 7) and surface area reduction (Fig. 8) predictions are shown, for a given pore geometry, for surface and gb diffusivites being doubled. An increase in gb diffusivity generates a proportional increase in through-thickness shrinkage, whereas the pore surface area reduction remains almost unchanged. An increase in surface diffusivity, on the other hand, accelerates surface area reduction. Pore

spherodization dominates, consuming the driving force for gb diffusion and hence reducing the shrinkage.

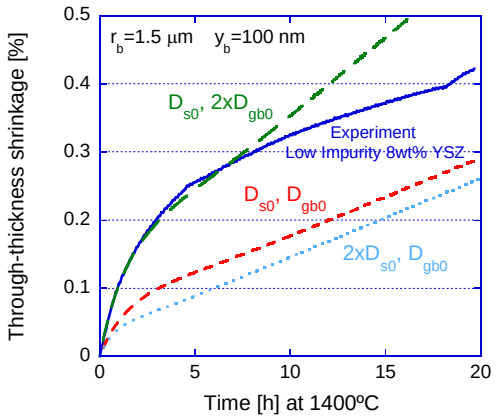

Figure 7: Predicted shrinkage in the through-thickness direction, showing the effects of changing gb and surface diffusivities.

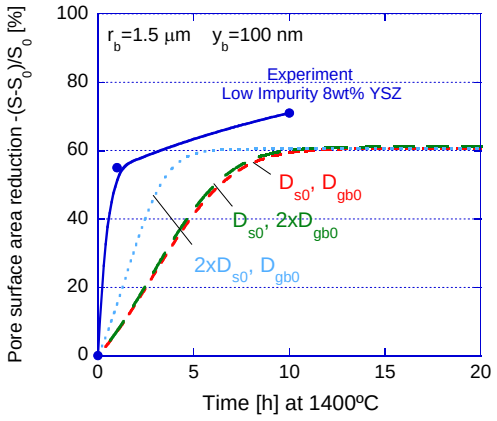

Figure 8: Predicted changes in pore surface area at 1400ºC, showing the effects of changing gb and surface diffusivities.

The geometrical representation used in the present work has been employed previously to predict the through-thickness thermal conductivity [2]. Figure 9 shows that the contact bridge to splat area ratio increases more rapidly with increasing surface diffusivity. Faster surface diffusion can thus accelerate the increase in thermal conductivity, while the rate of through-thickness shrinkage would be reduced. This indicates that the sintering behaviour cannot be fully described by shrinkage measurements and complementary information is required, such as surface area reduction and changes in pore size distribution.

Limitations of the Model

The presented version of the model is based on intersplat pores of uniform size. In practice, a distribution of pore size would be more appropriate. This would also account for intra-splat microcracks, with large surface to volume ratio, which can sinter quickly and may be the major contributors to surface area reduction. Other effects, such as grain growth, lattice diffusion, through-thickness thermal gradients and stresses due to constraint on sintering and thermal expansion mismatch with the substrate, should all be introduced into a fully comprehensive model. This is currently under study.

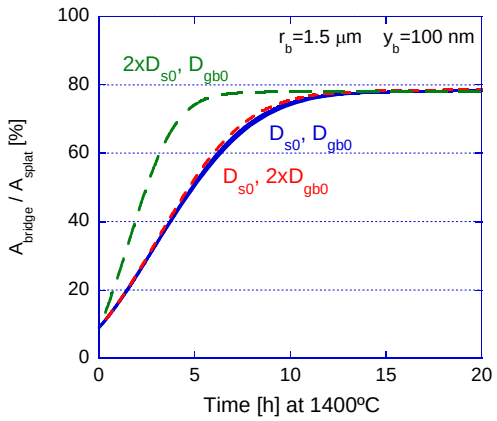

Figure 9: Predicted changes in contact bridge area at 1400ºC, showing the effects of changing gb and surface diffusivities.

Summary and Conclusions

A sintering model for PS TBCs has been developed, based on the variational principle. Input data, covering geometry and material properties, are obtained from experimental studies and include no arbitrarily-adjustable parameters. The model captures several well-established experimental trends and in general gives good agreement with experimental data and observations.

The sensitivity of predictions to initial pore geometry has been studied. Pores with larger initial surface area, but the same overall volume, lead to greater through-thickness shrinkage. Thus the initial porosity level does not dictate, or even strongly influence, the sintering behaviour. Moreover, pores with the same initial surface area, but different architecture (y_b to r_b ratio) lead to differences in the rate of surface area reduction. Architectures with fine inter-splat spacings (y_b) sinter faster and exhibit more rapid pore surface area reduction. However, the use of a single value for these dimensions is simplistic and a distribution of inter-splat spacing should ideally be incorporated into the model.

The sensitivity of model predictions to material properties has also been studied. An increase in gb diffusivity generates an approximately proportional increase in the rate of through-thickness shrinkage. Enhanced surface diffusivity, on the other hand, promotes pore spherodization and surface area reduction, consuming the driving force for gb diffusion and

hence cutting down the rate of through-thickness shrinkage. The model can also be used to predict the evolution of the inter-splat contact area, which can in turn be related to the through-thickness thermal conductivity, via a previously developed analytical model [2]. The increase in the contact bridge area is predicted to accelerate with increasing surface diffusivity. Faster surface diffusion is thus expected to raise the rate of thermal conductivity increase, while reducing the rate of through-thickness shrinkage. Of course, studying such effects experimentally presents challenges, since independently altering surface and gb diffusivities is not a simple matter, but these predictions do have implications for controlling the sintering characteristics and may be of practical significance.

Acknowledgements

Financial support has come from a Basque Government scholarship (for AC), from EPSRC via Platform Grant and from Sulzer Metco (US) Inc. The authors are also grateful for extensive useful discussions with Sulzer Metco personnel, particularly Mitch Dorfman, Clive Britton, Keith Harrison, Leon Xie and Jason Doesburg.

References

1. R.G. Hutchinson, N.A. Fleck, and A.C.F. Cocks, A Sintering Model for Thermal Barrier Coatings, *Acta Mater.*, 2006, 54(5), p 1297-1306.
2. I.O. Golosnoy, S.A. Tsipas, and T.W. Clyne, An Analytical Model for Simulation of Heat Flow in Plasma Sprayed Thermal Barrier Coatings, *J. Therm. Spray Technol.*, 2005, 14(2), p 205-214.
3. A. Needleman, and J.R. Rice, Plastic Creep Flow Effects in the Diffusive Cavitation of Grain-Boundaries, *Acta Metall.*, 1980, 28, p 1315-1332.
4. J. Pan, and A.C.F. Cocks, A Numerical Technique for the Analysis of Coupled Surface and Grain-Boundary diffusion, *Acta Metall. Mater.*, 1995, 43(4), p 1395-1406.
5. A.C.F. Cocks, and S.P.A. Gill, A Variational Approach to Two Dimensional Grain Growth - I. Theory, *Acta Mater.*, 1996, 44(12), p 4765-4775.
6. A.C.F. Cocks, Variational Principles, Numerical Schemes and Bounding Theorems for Deformation by Nabarro-Herring Creep,. *J. Mech. Phys. Solids*, 1996, 44(9), p 1429-1452.
7. Z. Suo, and W. Wang, Diffusive Void Bifurcation in Stressed Solid, *J. Appl. Phys.*, 1994, 76(6), p 3410-3421.
8. J. Svoboda, and H. Riedel, Quasi-Equilibrium Sintering for Coupled Grain-Boundary and Surface Diffusion, *Acta Metall. Mater.*, 1995, 43(2), p 499-506.
9. J. Pan, A.C.F. Cocks, and S. Kucherenko, Finite Element Formulation of Coupled Grain-Boundary and Surface Diffusion with Grain-Boundary Migration, *Proc. Roy. Soc. London A*, 1997, 453, p 2161-2184.
10. A.C.F. Cocks, S.P.A. Gill, and J. Pan, Modelling Microstructure Evolution in Engineering Materials, *Adv. Appl. Mech.*, 1999, 36, p 81-162.
11. M.J.M. Akash, Zr Surface Diffusion in Tetragonal Yttria Stabilized Zirconia, *J. Mater. Sci.*, 2000, 35, p 437-442.
12. Yoshio Sakka, Yasumichi Oishi, Ken Ando, and Shoji Morita, Cation Interdiffusion and Phase Stability in Polycrystalline Tetragonal Ceria-Zirconia-Hafnia Solid Solution, *J. Am. Ceram. Soc.*, 1991, 74(10), p 2610-2614.
13. R.N. German, *Sintering Theory and Practice*. 1st ed. (New York) John Wiley & Sons, 1996, p 534.
14. S. Brunauer, P.H. Emmett, E. Teller, Adsorption of Gases in Multimolecular Layers, J. Am. Chem. Soc., 1938, 60, p 309-319